

Celebrating Singularities: Mathematics and Chemical Engineering

Yunshan Wang, Xinguang Cheng, and Hsueh-Chia Chang

Dept. of Chemical and Biomolecular Engineering, University of Notre Dame, Notre Dame, IN 46556

DOI 10.1002/aic.14123

Published online May 8, 2013 in Wiley Online Library (wileyonlinelibrary.com)

The authors review and project their group's work in reaction engineering, electrokinetics, thin-film lubrication/wetting, biosensing, mass spectrometry, etc., that share one common mathematical underpinning: singularities. These can be geometric singularities of actual surfaces or objects, where focused electrical, acoustic, optical and shear-stress fields produce anomalous physical phenomena that have been explored mathematically with a spectral theory or exploited for specific applications. They are also singularities of mathematical manifolds, such as solution branches and Riemann manifolds, defined by abstract mathematical formulations, so that they can be used to design optical sensors, and understand nonlinear dynamical behavior that is relevant to system control and surface characterization. The common mathematical framework for these diverse topics underscores how mathematics can reveal, organize and inspire real and industrially relevant problems in chemical engineering. © 2013 American Institute of Chemical Engineers AIChE J, 59: 1830–1843, 2013

Keywords: microfluidics, reactor analysis, optics, biorheology

Introduction

The senior author fondly recalls his Associate Professor days at the University of Houston. It was a heady time in chemical engineering when mathematical analysis was respected and encouraged. Young faculty members were imbued with the excitement that, given the highly mathematical faculty at Houston, history would be made there. It would be the Göttingen of engineering, or at least chemical engineering. The intellectual orientation of chemical engineering has moved away from mathematical analysis recently. Theoretical articles often report molecular dynamics or fluid mechanics computations, with little analysis. It is the authors' collective opinion that this is a loss for our community at large—mathematical analyses can offer physical insight into an organization of complex phenomena in chemical engineering. Indeed, the best technologies can be inspired and guided by proper mathematics in the most elegant and yet precise manner. It supplies a common language that links our seemingly disparate disciplines, allowing knowledge to be transferred from one to another and inspiring insight in the new ones even when there is no apparent physical connection. Given the disparate length and time scales and complex integration of different materials/phenomena in current devices and processes, mathematics can offer a coherent, precise and rational description that is not accessible by computations, empirical approaches or human intuition. An intimate intertwine between

mathematics and relevant advanced technology is the ideal we would like to rekindle with this article.

A believer in this ideology, the senior author has strived to use mathematics in his work, however, applied, complex and diverse the project, to explain new phenomena in complex systems, to derive simple correlations and to invent new technologies for many fields in chemical engineering. He developed this style during his formative years at Houston. This short review/perspective reviews how mathematics was the common denominator that underpins his group's work (and guides its future direction).

The authors will refrain from an extensive review of steady-state and dynamic singularities in reaction engineering, which uses local theories to explore solutions near singularities of the solution manifold and was used to study steady-state multiplicity in exothermic reactions of nonbatch reactions, whose mass and heat exchange with the surrounding endows it with this and many other nonequilibrium phenomena impossible in closed systems near thermodynamic equilibrium. The senior author's own journey in this field started from his PhD thesis,¹ when he associated the solution surface of a first-order exothermic reaction in a CSTR to a cusp singularity (see Figure 1a) in catastrophe theory, where the singularity occurs on the manifold that is a map from the parameter space to the solution space. (His former colleagues at University of Houston would be more qualified to review this subject.) Nevertheless, the hysteretic behavior associated with the multivaluedness of the surface appears in many of the senior author's projects and so is the "ignition" dynamics associated with the transition from the lower manifold to the upper one, the two locally stable states for this bistable system. In fact, these diverse phenomena can be described by the same analysis because of the aforementioned similarities.

Contract grant sponsor: NSF; Contract grant numbers: IDBR0852741; CBET 1065652.

Correspondence concerning this article should be addressed to H. C. Chang at hsueh-chia.chang2@nd.edu.

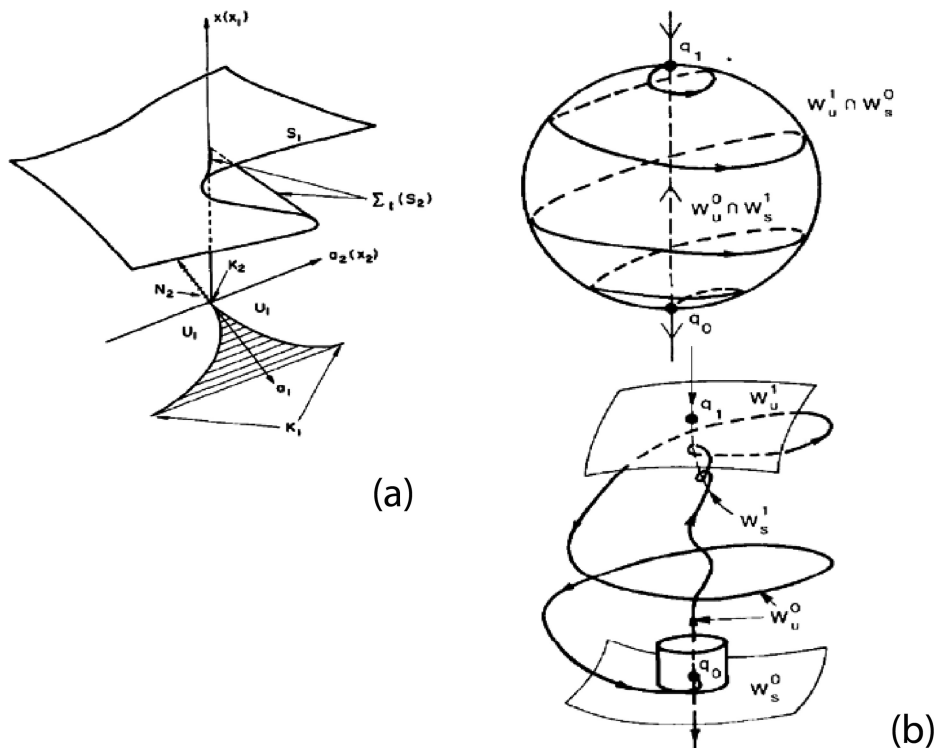


Figure 1. (a). The cusp Catastrophe for the solution manifold of a first-order exothermic reaction in a CSTR.

The shaded area in the two-dimensional parameter space is where 3 solutions (represented by x) exist. Ignition and extinction occurs at the boundary of the shaded region, and (b) solution trajectories near one singularity of a dynamical system derived from the Kuramoto-Sivashinsky equation for falling film waves. Shown in the bottom is the homoclinic orbit corresponding to a solitary wave.

A local expansion (sometimes called a center manifold projection) about the singularity on the manifold is equivalent to linearizing the problem and expanding about the dominant “zero” modes of the spectrum of the linear operator, eigenmodes with zero or purely imaginary eigenvalues, to capture how multiplicative parametric perturbation from the singularity and higher-order system nonlinearity excite the less dominant modes and, in turn, perturb the linear dynamics of the zero modes. Canonical low-dimensional dynamical systems for the zero modes produce equations like the Stuart-Landau and Ginzburg-Landau equations, which can describe many (but not all) physically different systems with the same singularity. Like the recent topological insulator theory in quantum mechanics, these zero modes are often related to certain symmetries in the system—geometric symmetries like translational and rotational symmetries as well as mathematical symmetries in the equation due to mass/energy conservation, etc. Sometimes both kinds of symmetries are connected. A well-known example in engineering of the latter symmetry is that a mass conservation related symmetry of the diffusion equation with respect to affine transformation allows a self-similar analysis of the diffusion equation and the convection-diffusion boundary layer.² Different classes of singularities from systems with different symmetries and different number of symmetries produce different normal forms; some of them are not as well-known as the GL equation. This tremendous reduction in system dimension, sometimes from infinity to less than three, allows a generic analysis (and understanding) of many systems with (often) closed-form estimates of the normal forms.

These closed-form solutions of the normal forms offer generalized correlations among dimensionless parameters familiar to the chemical engineers. The challenge is to find the proper singularities where the expansion can be valid over large spatiotemporal and parametric domains, and can classify as many solution features (topologies) as possible. It is, hence, quite similar in spirit to renormalization theories in physics where one strives to obtain a classification of different phase-transition critical points (singularity of the order parameter), and generalized phase diagrams with them as “organizing centers”. This is also the approach taken by unified field theorists, whose predicted Higgs particles were just recently detected. The senior author was able to use a dynamical version of the theory to explain different types of wave solutions on a thin falling film—he identified $(0,0)$ and singularities (two zero eigenvalues and one zero plus one imaginary pair) on the solution manifold where solitary wave, shock wave and periodic wave solutions of the Kuramoto-Sivashinsky equation converge in the parameter space.^{3,4} The solution manifold of the $(0, \pm i\omega)$ singularity is shown in Figure 1b. The purely imaginary pair suggests that time-periodic solutions exist in the neighborhood of such singularities. (In fact, a chaotic attractor also exists there and so do heteroclinic orbits (shocks) and homoclinic orbits (solitons).) The same dynamic singularity theory was used to analyze high-Reynolds number vortex formation and instability in several packed bed models.⁵ The earlier wave work led to a 10-year analysis of wave dynamics on a falling film, mostly with Evgeny Demekhin.⁶ The “turbulent” thin-film wave dynamics were shown to be dominated by a

ubiquitous “coherent structure”—the solitary waves. Hence, one can examine how solitary waves interact with each other⁷ through zero modes that arise from translational invariance of the solitary waves and how solitary waves interact with wave fields⁸ with a special weighted spectral theory to reveal another zero mode related to mass conservation. Using such dynamic singularity theory, they are able to decipher the complex wave dynamics over a large domain with simple correlations derived from low-dimensional dynamical systems. Similar approaches were used to study wetting patterns,⁹ nanoscale pattern formation in electropolishing¹⁰ and nanopore formation in anodization.¹¹

However, the aforementioned mathematical works, however sophisticated, do not lead to new technologies. The senior author’s first industrially relevant theoretical work came with his realization that the reason it is difficult to implement P and PI control on underdamped systems with delay is that it often has two distinct cross-over frequencies—a double Hopf singularity¹²($i\omega_1, i\omega_2$). Guided by the theory, his group was able to produce two-frequency oscillations (a so-called torus attractor) in a CSTR flow control experiment, using the conventional Ziegler-Nichols empirical tuning approach and, thus, demonstrating it is invalid for such systems. They have also used the same singularity theory to reduce the dimension of distributed systems such that low-order control strategies can be implemented.¹³

This review/perspective will focus on the group’s work that has very specific and direct industrial relevance—they result in new technologies and new patents from the authors’ group. The singularity theory used in the work offers reduced models with closed-form or nearly analytical correlations that were fruitfully used to understand the complex phenomena and arrive at the new designs. The theme is that, although the efforts span the entire wide spectrum of chemical engineering and encompass both classical and cutting-edge technologies, they are fundamentally connected through singularity theory—knowledge from one effort has been fruitfully used in another in a way unique to mathematics. Not all the senior author’s attempts to use mathematics to improve technology have been successful. For example, his earlier work of using dynamic singularity theory to produce chaotic mixing for heat-transfer enhancement led to a patent,¹⁴ but its efficiency is far lower than what can be achieved with clever designs with tortuous flow geometries that can regenerate thermal boundary layers or produce vortex shedding.¹⁵ The thermal Peclet number is so high that passive chaotic mixing can never compete with convective heat transfer in open-flow system. However, even in failed examples, knowledge is gleaned and passed down to future generations in a concise, rigorous and elegant manner that befits a proud and inventive discipline.

Designing Fast-Igniting Catalytic Converters

In the 1990s, before the appearance of high-revolution and high-efficiency engines with a much hotter exhaust gas, the temperature of the exhaust gas entering the catalytic converter is at about 600 K for a car driving on surface roads at 35 miles/h. Although CO and NO_x in the exhaust can still be removed at this temperature, hydrocarbons require the catalytic converter to ignite (a trajectory that takes off from the lower manifold to the top in Figure 1a), and its temperature rises beyond 900 K from the heat released by the highly exothermic CO oxidation reaction. It was found through

extensive simulation by the General Motors reaction engineering group and by the senior author’s group that, with the exhaust composition and temperature from the automobile models then, the three-way ceramic monolith catalytic converter would not ignite under a standardized cold-start and surface road driving conditions unless the exhaust temperature¹⁶ increases to 800 K. The elevated exhaust temperature can be achieved when the car accelerates to highway speeds. For cars on surface roads or congested highways, the catalytic converter essentially remains unignited over the average commuting drive of about 20 min, with all its HC pollutants released to the environment. It was realized very early, through extensive simulation at the GM supercomputer, that the reason for this slow converter light-off at low speeds is that, at low-exhaust temperatures such as 600 K, the converter first ignites at the downstream end, forming a localized hotspot there. The heat released from that hot spot is convected out of the exhaust pipe instead of heating the rest of the converter upstream to ignite the entire converter. Earlier remedies such as using a metallic monolith (Corning, W R Grance and Allied Signals) to conduct heat upstream from the downstream ignition point, using a preheater and to increase the catalyst load at the upstream end of the converter all fail due to a poor understanding of the underlying mechanism or to manufacturing or cost constraints.

In an article with David Leighton,¹⁷ the senior author pointed out that hydrodynamic thermal dispersion could shift the ignition position from the trailing end to the leading end of the catalytic converter, such that the heat released can be used to heat up the rest of the converter. The exhaust gas thermally heats up the cold monolith such that a thermal front propagates along the solid monolith at a thermal velocity U_{eff} that is much smaller than the gas exhaust velocity U due to the far larger thermal capacitance of the monolith. A simple capacitance averaging yields $U_{eff} \approx U/\gamma$ where $\gamma \gg 1$ is the ratio of the solid thermal capacitance to that of the gas. However, due to imperfect thermal equilibration between the two phases, the thermal front suffers from dispersion, much the same way as hydrodynamic Taylor-Aris solutal dispersion, with an effective thermal diffusivity, normalized by the gas thermal diffusivity, that scales as the square of the Peclet number (see physical arguments for this Taylor scaling).¹⁸ Quite counterintuitive to the uninitiated is that the effective dispersion scales inversely with respect to the molecular diffusivity). There is an extra capacitance ratio that factors into thermal hydrodynamic dispersion, since unlike solutal transport, heat transport permeates into the entire solid phase. The effective thermal diffusivity scaled by the gas diffusivity is then $\alpha_{eff}/\alpha_g \sim Pe^2/\gamma$, where the thermal Peclet number is $Pe = Ua/\alpha_g$, where $a = 0.06$ cm is the standard monolith pore size, and $\gamma = 2000$ is the large thermal capacitance ratio between solid and gas. With the fast gas flow ($U \sim 2 \times 10^2$ cm/s), the Peclet number is large in excess of 100, and the effective thermal diffusivity α_{eff} is about half of the large gas thermal diffusivity $\alpha_g = 0.74$ cm²/s, and about 100 times higher than the solid thermal diffusivity. Due to the large capacitance (thermal velocity) ratio, the solid thermal diffusivity contribution to effective thermal dispersion is insignificant, explaining why metal catalytic converters are bad ideas. Whether the ignition occurs at the downstream or upstream end of the monolith then depends on whether dispersion can lower the front temperature sufficiently to suppress ignition at the downstream end. It is, hence, determined by the magnitude of a key parameter

$\chi = (\alpha_{eff}/U_{eff}^2 t_{ig}^\infty)$ that is equal to the thermal dispersion time of the front α_{eff}/U_{eff} and the kinetic ignition time without thermal transport or flow t_{ig}^∞ , which is about 17 s for a monolith at 300 K that is exposed to a step increase in the exhaust temperature to 600 K. It was estimated numerically that χ must be unit order or larger for thermal dispersion to prevent downstream ignition. It was also estimated that, at standard conditions, the monolith is just below the required value. It was, hence, important to estimate accurately α_{eff} beyond just a simple scaling theory, without doing extensive numerical simulation or even worse, extensive prototype building, to cover the myriad of design parameters.

At about the same time, in an article with Vermuri Balakotaiah, the senior author realized that dynamic singularity theory (in the form of center manifold projection) could be used to reproduce the classical Taylor-Aris dispersion coefficients for solutes.¹⁹ Its mathematical formalism due to different versions of center manifold projection is much simpler than the moments method used before that work. Dispersion is a transient phenomenon that can only be defined when thermal or solutal diffusion in the cross-flow direction is much faster than convection in the flow direction. Since the Peclet number Pe based on the transverse length scale is often large, this implies that one must consider a convection length scale L_∞ in the flow direction that is much larger than the transverse length scale $L_\infty/a = 1/\varepsilon \gg 1$ for the catalytic converter, since its thermal Peclet number is large $Pe \gg 1$. (Dispersion only occurs after a length scale L_∞ that is much larger than the transverse length scale.) As such, if one scales the transverse coordinate by a , and the longitudinal coordinate by L_∞ , which can be taken to be the length of the standard monolith at 14.7 cm, and take the limit of $\varepsilon \rightarrow 0$, one gets a transient diffusion equation in the transverse direction. If the domain is insulated, this diffusion operator has a spectrum with a discrete zero eigenvalue. The formalism offered by the center manifold theory then projects the higher-order convection terms onto the eigenspace of the zero modes to couple the effects of convection with dispersion. The result is that the convection-diffusion equation in two spatial dimensions is reduced to a convection-diffusion equation in one-dimension (1-D), with an effective dispersion

$$\frac{\partial T}{\partial t} + U_{eff} \frac{\partial T}{\partial x} = \alpha_{eff} \frac{\partial^2 T}{\partial x^2} + \frac{e^{\beta(T-T_g^{in})}}{\beta t_{ig}^\infty} \quad (1)$$

where T_g^{in} is the temperature of the exhaust, and β is the inverse Frank-Kamanetskii temperature that estimates the ignition temperature of the exothermic reaction. The simple exponential dependence on scaling represents a kinetic model reduction of the full kinetics, with its different reactant and product species, and its complex temperature dependence at the ignition fold point of the cusp singularity in Figure 1—on the catalytic converter's solution manifold. The effective thermal dispersion term for the catalytic converter, however, requires expansion about another singularity—the zero mode of the diffusion equation. Several projection methods have been developed for this projection. Under certain conditions, Leighton and Chang¹⁷ are able to use an infinite series expansion to obtain an explicit estimate of $\alpha_{eff}/\alpha_g = (11/48)(Pe^2/\gamma)$ for a cylindrical pore approximation of the square monolith

pore. It is a remarkably simple correlation for such a complex system.

Substituting this effective thermal diffusivity into the projected simple 1-D convection and diffusion equation and with some asymptotic analysis¹⁷ a solution to Eq. (1) is obtained and it offers a simple correlation-like estimate of the ignition time

$$(t_{ig}/t_{ig}^\infty) = 1 + 2\chi^{1/2} |\ln(\chi^{1/2}/2\eta)|^{1/2} \quad (2)$$

where $\eta = \beta(T_g^{in} - T_s^0)$ is the difference between the inlet exhaust temperature $T_g^{in} = 600K$ and the initial monolith temperature of under standard conditions, normalized by the inverse Frank-Kamanetskii temperature β . The ignition location is estimated by $L_{ig} = U_{eff} t_{ig}$. It is clear from Figure 2a that this analytical estimate offered by dynamic singularity theory can accurately capture the numerical value from brute-force simulation of this complex system.

It is seen that upstream ignition occurs for $\chi > 0.5$, and the standard condition and monolith design yields $\chi = 0.13$. The question is then how one can redesign the catalytic converter to increase χ by a factor of 4. After weighting several design strategies against costs and fabrication difficulties, Keith et al¹⁶ arrived at the condition that preheating the exhaust to increase t_{ig}^∞ is the only viable means of χ increasing to the desired value with the standard exhaust conditions. One design, shown in Figure 2b, is to use a short converter upstream as a preigniter and bypassing a fraction of the

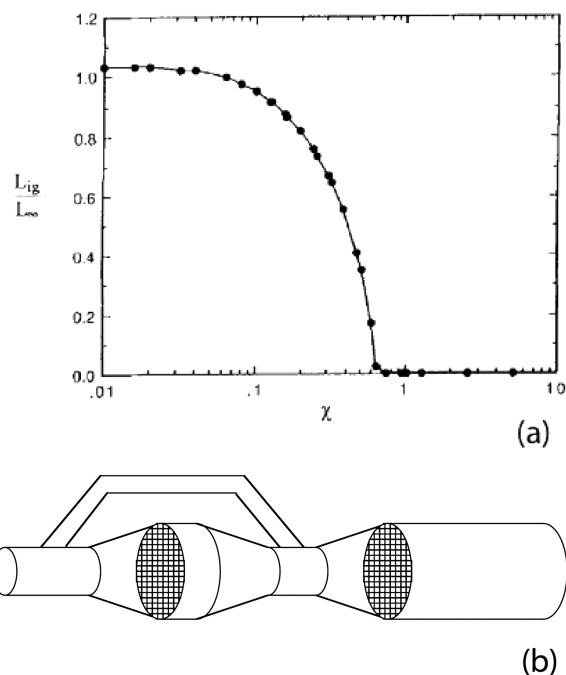


Figure 2. (a) Comparison of the ignition location $L_{ig} = U_{eff} t_{ig}$ as a function of the parameter between the curve from analytical theory of Eq. 2 and the solid data points from numerical simulation for a single catalytic converter.

The parameter χ is a ratio between ignition time and dispersion time, and (b) A 2/3 bypass design with a short converter as preigniter. The flow through the preigniter is turned off after the main converter downstream lights off. This design has been shown to ignite in 10 s under transient standard testing protocols.¹⁶

exhaust—the unignited main converter still offers satisfactory CO and NO_x conversions. The exact ignition location of the preigniter is inconsequential and given the required exhaust temperature of 800 K at highway speeds for light-off, only 1/3 of the exhaust needs to pass through the preigniter. This third bypass would be switched off when the main converter has ignited. This and other designs have been shown to offer consistent rapid ignition within 10 s—soon after the car leaves the driveway and without accelerating to highway speeds.¹⁶ It is difficult to imagine that such a simple design for such a complex problem can be achieved without the reduced model and its analytical solution offered by singularity theory, thus, eliminating or reducing confusing, inaccurate and largely unnecessary numerical and empirical search. A rather straightforward extension from solutal to thermal dispersion allowed the transfer of knowledge and mathematical machinery from the former to the latter to produce a viable design. The aforementioned bypass design is the basis of a Notre Dame patent²⁰ and is in some European automobiles. With fuel injection control in modern engines, the exhaust temperature is sufficiently high so this bypass design is not necessary. However, the need may arise again if diesel engines and engines for other alternative fuels become more common. The mathematics should be equally useful for many current and future light-off problems, even if the parameters or even systems are different—such is the power of a general mathematical framework. For example, diesel engines are extremely polluting and the modern diesel emission system includes a soot particulate trapping and burning procedures. We refer the readers to J M Keith's excellent articles on this subject,²¹ which contains in-depth mathematical analysis of the relevant thermal dispersion phenomena.

Designing More Sensitive Mass Spectrometers

The same analysis applied to the singularity of a solution manifold can also be used to analyze actual geometric structure with a surface or volume singularity. The best example of an industrially relevant geometric singularity is the Taylor cone for proteomic mass spectrometry. It is difficult to ionize proteins for analysis in a mass spec because the biomolecules prefer to remain in water and it is difficult to ionize the proteins in water and create nano-sized drops for injection into the mass spectrometer. Before this need was even appreciated, Taylor had realized that when a sufficiently high-direct current (DC) electric field is applied to a liquid drop at the end of a capillary, it deforms into a conic structure now called a Taylor cone.²² In typical practice, the tip of this cone extends to form a liquid microjet (cone-jet mode), and charged nanosized droplets are ejected from the tip.²³ John Fenn then showed that molecules in the Taylor cone can be ionized at a particular voltage so that the charged droplets contain ionized molecules and can be easily transmitted into a mass spectrometer. This electrospray ionization has become a workhorse in proteomic mass spectrometry because it enables soft ionization of proteins from an aqueous solution.²⁴ However, the droplets are ejected in a large, expanding plume that negatively impacts transport into a mass spectrometer, with injection efficiencies²⁵ less than 1%. Moreover, the size and charge of each aerosol directly influences the all-important degree of ionization of the analyte molecules within the droplets.

Yet, despite more than 50 years of theoretical scrutiny and 20 years of extensive use in mass spectrometry, the underlying mechanisms behind microjet breakup and plume formation remain unknown.

Taylor²² offered the first mathematical description of the conic meniscus singularity for an electrospray, which has been studied experimentally since the pioneering work of Zeleny.²⁶ Taylor's theory omits the microjet and assumes the meniscus cone is a perfect singularity. He solved for the harmonics of the Laplace equation near the constant-potential cone, stipulating that the Maxwell electric pressure that results from the local potential distribution must match the singular capillary pressure γ/r of the cone, for a surface tension of γ_f , due to its azimuthal curvature. Solving the spherical harmonics near a cone is a spectral problem in the radial coordinate r and the “zero modes” here correspond to discrete eigenvalues whose total electric energy remains finite. The dominant mode under this constraint has a potential φ that scales as $r^{1/2}$ and a singular electric field $E = -\nabla\varphi$ that scales as $r^{-1/2}$, with a corresponding Maxwell pressure $\epsilon_o|\nabla\varphi|^2$, where ϵ_o is the gas permittivity, that scales the same way in the radial coordinate as the singular capillary pressure of a conic free surface. This simple argument selects the dominant spherical harmonic of $r^{1/2}P_{1/2}[\cos(\pi-\theta)]$ for the potential near the cone, with a Legendre function P_n of order $n=1/2$ in the polar angle θ direction, and the requisite $r^{1/2}$ in the radial direction. In fact, one of the authors computed other harmonics for an isopotential cone and found a countably infinite of them (see Figure 3b). Nevertheless, the Taylor mode is the most singular mode—it is the dominant zero mode that dominates the electric potential distribution near the cone. This zero mode must satisfy the boundary condition that it vanishes at the cone half-angle because of the equipotential condition on the conducting or high-permittivity cone interface. Taylor then obtained a universal cone half-angle of $\theta = 49^\circ$ for any high-permittivity (or high conductivity) liquid cone. The Taylor cone is a very elegant real-life example of a dominant discrete and singular (in gradient) mode in (semi-) unbounded domains that can only occur near geometric singularities, such that the local electric field has a generic functional dependence that is insensitive to far-field conditions.

There is, however, a fallacy to Taylor's argument. Real cones are not perfectly sharp and are actually rounded off by a spherical cap with a radius of curvature. The capillary pressure of this spherical cap is $2\gamma/a$ and yet the spherical harmonics for the electric potential near the spherical cap is $1/r$, giving rise to an electric field at the rounded tip that scales as a^{-2} and a Maxwell pressure that scales as a^{-4} . Hence, in the limit of $a \rightarrow 0$, matching of capillary and Maxwell pressures becomes impossible at the rounded tip. A new physical phenomenon not described in Taylor's theory must, hence, exist at the cone tip. In recent experiments from the authors' laboratory, this new physical phenomenon is found to be the microjet that emits from the Taylor cone. In fact, it is suspected that the Taylor cone cannot exist without this microjet. Moreover, as seen in Figure 3a, the submicrom droplets are formed when the microjet explodes dramatically and ejects a conic plume of nanodrops. This conic geometry of the ejected aerosol plume is, in the authors' opinion, why electrospray mass spectrometry has only 1% injection efficiency. A current effort in their laboratory is to understand the charging of the microjet and the

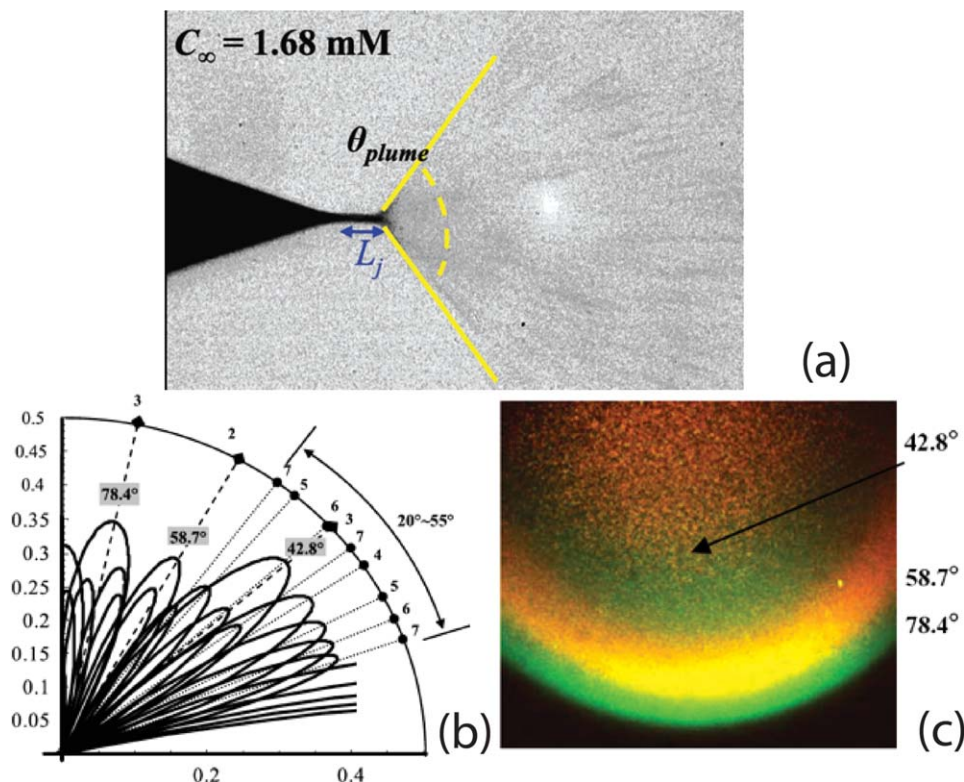


Figure 3. (a) Image of the Taylor cone, microjet and aerosol plume, (b) the field maxima from the Taylor cone that controls the aerosol plume, and (c) nanocolloids of different size (980 nm, 400 nm and 200 nm) are ejected in different member of a nest of concentric conic plumes and are deposited as semicircles on the substrate.

[Color figure can be viewed in the online issue, which is available at wileyonlinelibrary.com.]

mechanism behind the conic plume explosion. Fortunately, the dominant Taylor potential $r^{1/2}P_{1/2}[\cos(\pi-\theta)]$ dominates the polarization/charging of the microjet and simple analysis can provide estimates for the length of the microjet and the aerosol plume cone angle.²⁷ The cutoff mechanism for a geometric singularity is often of utmost importance but one can still use the dominant zero mode without the cutoff to analyze the physics of the cutoff. The mathematical approach is quite similar to how center manifold projection handles a parametric perturbation around a singularity on the solution manifold.

The observation that the zero-mode Taylor potential $r^{1/2}P_{1/2}[\cos(\pi-\theta)]$ for the cone still dominates the potential around microjet allows us to estimate the angle of the conic plume emitted from the microjet and the trajectory of any molecule within the plume. This theory is validated by empirical measurements of the trajectories and deposition patterns of nanocolloids of different size when they are ejected at the plume.²⁸ Because the dominant field due to the Taylor potential is in the axial direction along the jet, the transverse force on the nanocolloids is due to Coulombic repulsion between the colloid and the charged jet, which is dependent on the colloid size. The net result is that nanocolloids of different size are ejected in different conic plumes and deposited as concentric rings, as seen in Figure 3c. These concentric conic plumes were shown to correspond to higher harmonics of $r^m P_m[\cos(\pi-\theta)]$, which still satisfies the equipotential condition at the Taylor cone $r^{1/2}P_{1/2}[\cos(\pi-49^\circ)]=0$. The modes $m=3.275$, and 4.655 are the next dominant modes with field maxima less than

90° , at $=58.7$, 42.8 and 78.4° . The first is the lone field maximum of mode $m=3.25$, and the latter two the two maxima of mode $m=4.655$. The three concentric rings of deposited nanocolloids in Figure 3 correspond to these three plume angles. The group and their collaborators have used this unique mathematical feature of the dominant discrete modes near the Taylor cone, including the Taylor mode $m=1/2$, to design a nanocolloid mass spectrometry that can separate nanocolloids of different size. A pending patent is on how such a method can be used to quantify the number of nanocolloids with bound biomolecules, biomarkers that the nanocolloids have captured with specific probes functionalized onto them.²⁹

The Maxwell pressure $\epsilon_0|\nabla\phi|^2$ that is produced by the Taylor potential near a cone is produced by dielectric polarization—field-induced interfacial charge on the interface due to molecular polarization by the DC field. However, this is not the only electric pressure that is possible. The dramatic explosion of the microjet in Figure 3a, and the Coulombic repulsive force between nanocolloids in Figure 3c suggest that net space charge, not induced charge, on the interface can produce an electric pressure different from the Maxwell pressure. By using an AC field at high frequency (>100 kHz), such that high-mobility cations (protons) generated by ionization reaction in the meniscus tip can relax into the bulk but not the low-mobility anions, the authors' laboratory was able to accumulate net space charge at the meniscus tip. The result is an AC cone with a universal angle of 11° instead of the Taylor angle of 49° due to induced dielectric polarization,³⁰ as seen in Figure 4a. Nishant Chetwani of the

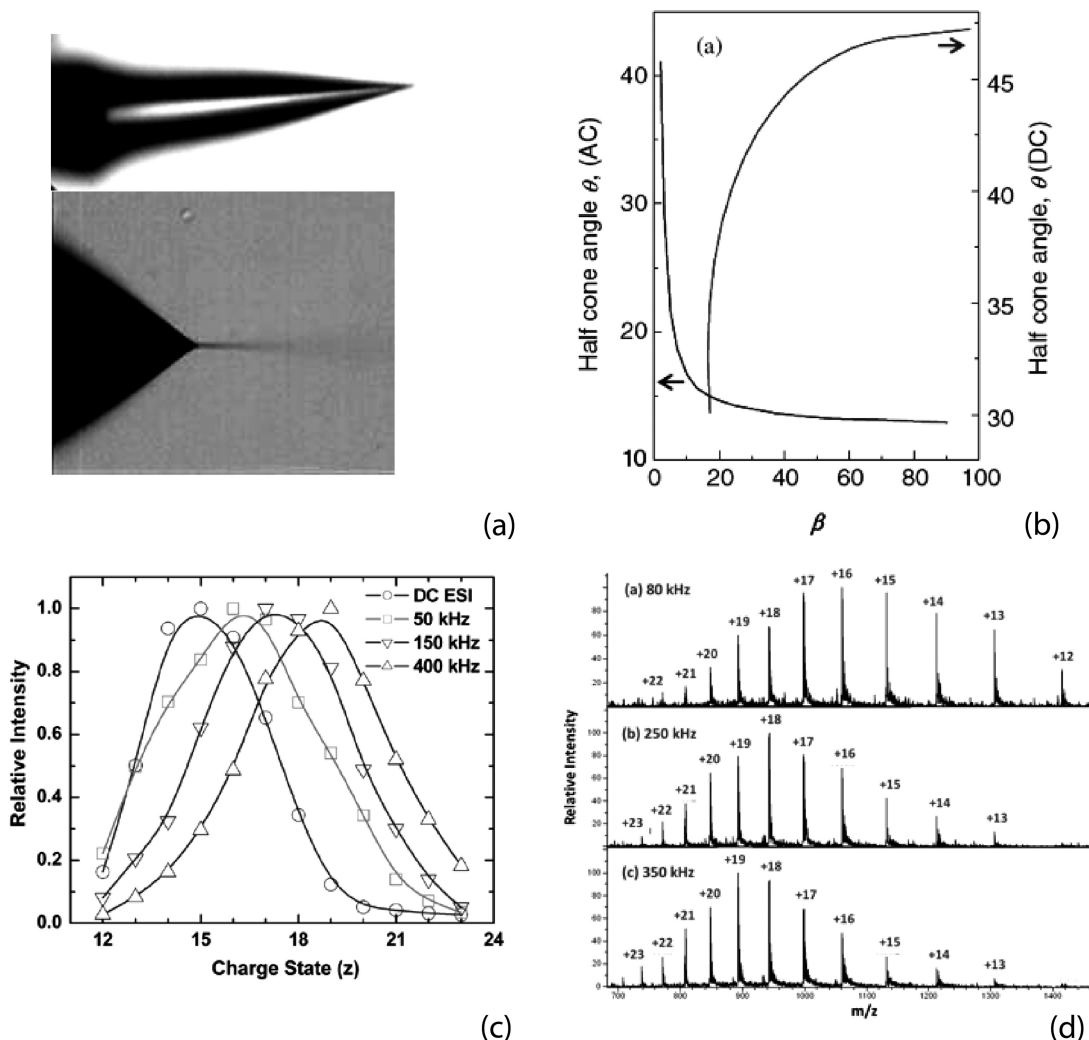


Figure 4. (a) The distinct difference between an AC cone with an 11° half angle and a DC Taylor cone with a 49° half angle, (b) theoretical analysis of the DC (top curve) and AC (bottom curve) cone angle as a function of the ratio of liquid permittivity and gas permittivity.

The DC Taylor theory is based on the dominant mode from the spectral analysis of the Laplace operator with induced charge (displacement) boundary conditions. The AC theory is based on a variational analysis of space charge Coulombic repulsion. Note the different dependence on β , (c) the charge state of the apomyoglobin mass spectrum at different frequencies of the AC spray and for DC spray, and (d) mass spectra at different frequencies, showing the shift to higher charge states at high frequencies.

authors' laboratory formulated a variational theory to describe the electric energy due to Coulombic interaction of this interfacial charge, which was able to accurately capture the observed angle of 11° .³⁰ His analysis was simplified by the observation that the resulting pressure must scale as $1/r$, since it must also balance the cone capillary pressure of the same scaling, as was first observed by Taylor. The mass spectrometry due to this AC electro-spray is quite distinct from DC spray, as the pH of the sample can be tuned by just changing the frequency near the inverse diffusion time of protons and that the anion can be concentrated at the tip.³¹ The charged state of an analyte is seen to be a function of the AC frequency, as seen in Figure 4c. This pH control and other unique features of AC spray have been used in several new AC electrospinning technologies.^{32,33}

Instead of relying on the electric field to produce a meniscus with a conic singularity, one can also use an existing wedge geometric singularity of a contact line to focus electric field and acoustic waves. Gagnon and Chang have used this technique to generate nanobubbles and nanodrops at a

contact line.³⁴ This concept also led to the development of surface acoustic wave mass spectrometry.³⁵ The surface acoustic wave on the piezoelectric surface scatters into the interior of a liquid drop lying in its path. The scattered bulk acoustic wave generates submicrometer drops at the end of the drop. The electric field of the piezoelectric device is also focused at the contact line where the scattering occurs, ionizing any molecule at that region. The result is an alternative ionization and atomization method for mass spectrometry. Preliminary results indicate the ionization is much softer than DC or AC sprays.

Designing More Sensitive and More Rapid Biosensors

That an electric field is focused at geometric singularities can be used to improve many bioassays. Pull-down surface assays, like the DNA microarray, involve surface-functionalized probes like antibodies or single-stranded oligonucleotides that can capture specific target molecules like proteins

and complementary nucleic acids, respectively. However, for practical samples, such docking or hybridization reactions are often transport limited. The diffusion time of the target molecules often exceeds hours for practical samples, which is much longer than the reaction time. Convective mixing can reduce this time but since the mass-transfer Peclet numbers cannot be large in biochips, the diffusion-convection boundary layer is often comparable to the chip height. Consequently, another more short-range force on the target molecules is needed to transport them faster to the surface probes. The authors' laboratory has found that nanometer-sized large biomolecules like nucleic acids have very large dielectrophoretic (DEP) mobility because of ion polarization within the Debye layers.³⁶ The DEP mobility scales $|\nabla E|^2$, and, hence, is largest near geometric singularities with singular electric fields like conic structures or pointed electrodes (see Figure 5). Another way to generate near-singular electric fields is through fabrication of nanoslots^{37,38} and through assembly of nanocolloids.³⁹ In Figure 5, DNA molecules are shown to be attracted to a nanocolloid assembly with high fields within 1 min by DEP (compared to the hour-long diffusion time) with this mechanism. Several patents from the authors' laboratory involve different designs for this DEP molecular transport to reduce the assay time of biosensors. The hybridization of the target molecules onto probes on the biosensor can then be reported optically (fluorescence, absorption or Raman scattering^{39,40}) or electrochemically.^{41,42} In some cases, the DEP mobility and even direction are different for different molecules or for nanoscale floating electrodes like carbon nanotubes and nanocolloids with or without hybridized molecules. In such cases, selective transport can also be achieved.^{41–45}

Center manifold projection also allows us to derive the effective AC ion conductivity of nanocolloids. Since electromigration and electro-osmotic convection exist within the Debye layer, which is much thinner than nanocolloid size, dispersion effects are important and an effective tangential transport equation, much like the effective thermal dispersion of catalytic converter under transient conditions in Eq. (1), can be derived⁴⁵ to produce a closed-form expression for the effective ion conductivity for the nanocolloids. The "surface" conductance within the Debye layer can render a dielectric latex nanocolloid conducting, with nearly metallic conductivity because of the high-ion concentration within the Debye layer. This ion polarization mechanism dominates DEP at frequencies below the inverse ion dispersion time along the double layer and it produces an induced colloid dipole that is in opposite direction compared to dielectric (molecular polarization) at high frequency. This implies that the DEP transport of the nanocolloids can switch from negative DEP (toward low fields in a biochip) to positive DEP (toward high fields) upon molecular hybridization. This DEP molecular spectroscopy must be carried out near crossover frequency, which is $\omega_{co} = \frac{\sigma_p}{2\sqrt{2\pi\epsilon_m}}$, where ϵ_m is the medium permittivity, a the colloid size, and the effective nanocolloid conductivity for a dielectric nanocolloid is $\sigma_p = 2K_s/a$ from the theory,^{36,45} with the surface conductance being related to the surface charge density $\sigma_s K_s = DF\sigma_s/RT$. The validity of this simple correlation, derived from singularity theory, is verified by successfully collapsing crossover frequency data for a range of particles with different charge density and in different ionic strengths, as seen in Figure 6. The hybridized molecules change the surface charge density, which alters

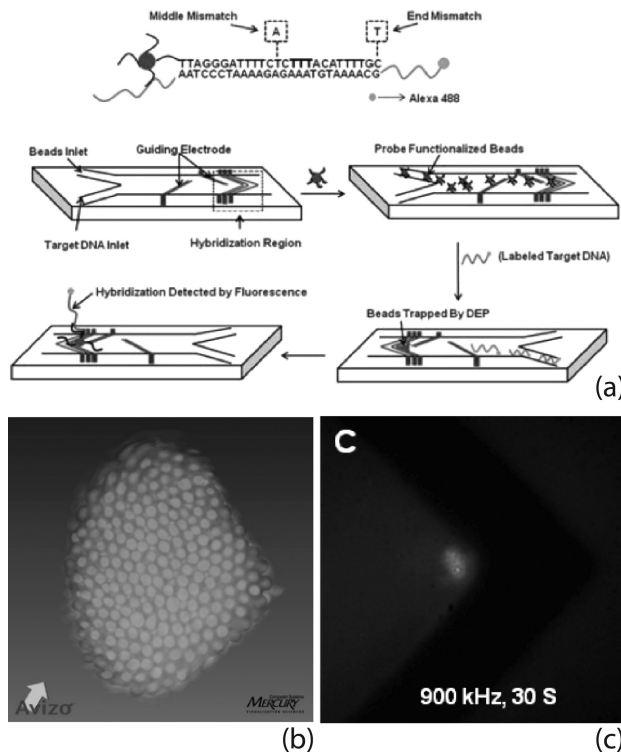


Figure 5. Multiscale dielectrophoretic traps.

(a) Pointed electrodes with high-intensity AC field is used to assemble nanocolloids with functionalized nanobeads from a flowing suspension, (b) the assembled nanobeads with highly focused electric fields at its interstices, particularly at the pointed end near the tip of the arrowhead shaped electrodes, and (c) fluorescent DNA molecules are trapped at the tip of nanocolloid assembly within 1 min.

the ion concentration within the Debye double layer, and, hence, the ion conductivity of the nanocolloids. This peculiar Debye layer conductance endows a very unique size and surface charge dependence of the DEP crossover frequency of nanocolloids that can be used to quantify the number of molecules on the nanocolloids, sometimes even to determine conformation of the hybridized molecules.⁴⁶ Note that the surface charge effect can only be captured for nanocolloids roughly between 10 nm and 500 nm.

Optical fields can also be focused by geometric singularities. However, such focusing only exists for plasmonic (surface) electromagnetic waves on metallic cones, as bulk radiation actually scatters off dielectric cones. The authors' group is developing a discrete spectral theory for the former and a new spectral theory to describe the essential spectrum responsible for bulk radiation scattering off dielectric cones.⁴⁷ We report some preliminary results for etched optical fiber tips. Such tips can be coated with a gold film to sustain plasmonic waves. The same gold film can be electrically activated to use electrical DEP to rapidly transport the target molecules to the tip surface. However, we shall focus here on the focusing of plasmonic waves to the gold tip here as a means of reporting the presence of hybridized target molecules there.

The cone harmonics now correspond to the spherical harmonics of Maxwell equations. We solve the full Maxwell equations for localized EM field at the tip of an infinite long cone in spherical coordinate. The apex angle of the cone is

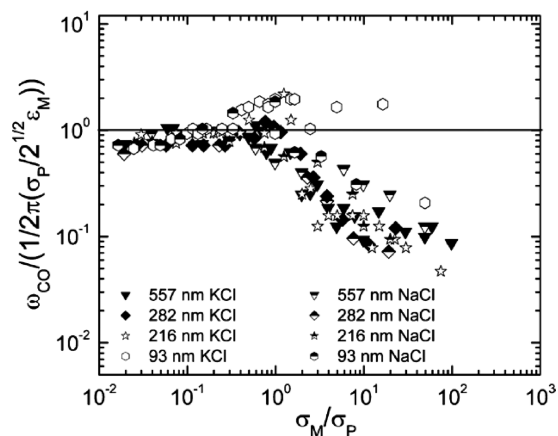


Figure 6. Collapse of latex nanocolloids DEP crossover frequency data for different nanocolloid size and different ionic strengths of different media.

The theory is provided by averaging over a dominant mode to produce an effective transient nanocolloid ion electric conductivity.

2α and the cone is made of a material with a complex permittivity ϵ_m , and a permeability μ_m surrounded by a dielectric medium with a real permittivity ϵ_o and a permeability μ_o . Applying the continuity of the field and displacement on the interface and omitting higher-order less singular plasmonic modes, a transcendental dispersion relationship is obtained for the dominant eigenvalue v , $\frac{\epsilon_m + f(\pi-x,v)f_0(x,v)}{\epsilon_o + f(x,v)f_0(\pi-x,v)} = \frac{\epsilon_m}{\epsilon_o} + g(\alpha, v) = 0$, with $f(\theta, v) = P_v^1(\cos \theta) \sin \theta$. In near field the radial component of the electric field $E_r \sim r^{v_r + iv_i} = r^{v_r - 1} e^{iv_i \ln r}$ ($v = v_r + iv_i$, r is the radial distance from the apex of the cone), while the azimuthal magnetic field H_ϕ is less singular since it scales as r^v . Note that while field singularity occurs in the radial direction of the spherical coordinate, both electric and magnetic field decays in the azimuthal polar direction. We define $1 - v_r$ as the intensification exponent as it is related to the amplification of the electric field as the azimuthally confined plasmonic radiation focuses to the tip. The restriction that the total EM energy be finite over the entire domain⁴⁸ requires that $v_r > -1/2$. The position-dependent wave number $\kappa = v_i/r$ increases dramatically as plasmon waves propagate toward the tip, which is found to be negative ($v_i < 0$) for the converging waves with speed retardation.

The plasmonic dispersion relationship defines a conformal map from the complex permittivity space to the complex eigenvalue space, as shown in Figure 7a, and the inverse conformal map is shown in Figure 7b. The branch point ($v_r = -1/2, v_i = 0$) on the intersection of two Riemann sheets (shown as the black circle in Figure 7a) has significant physical implications—it corresponds to the demarcation line between bounded and unbounded total electromagnetic energy for the cone. At this point, the analyticity of the dispersion relationship coincides with energy conservation criterion. To sustain surface plasmon waves, other than the global energy conservation criterion, negative real permittivity and positive imaginary permittivity of the metal must also apply. Negative real permittivity is a prerequisite for surface bounded waves, and positive imaginary permittivity guarantees that waves converge to the tip, instead of diverging to the far field. Therefore, only the dark region of the

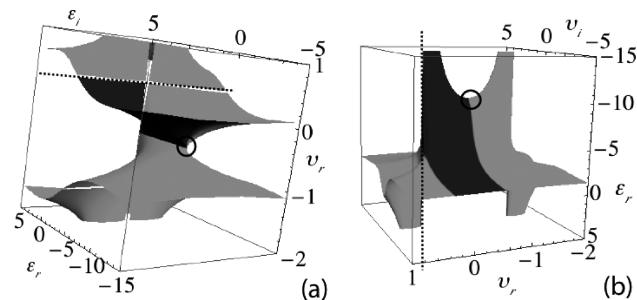


Figure 7. (a) Conformal map of dispersion relation, where the circle marks the branch point, and the dashed line marks where v_r goes to infinity.

The dark region is where surface plasmon waves can be excited, (b) Inverse conformal map of dispersion relation, where circle marks the image of the branch point and the dashed line marks where v_r goes to infinity. The dark region is where surface plasmon waves can be excited.

Reimann sheet can sustain surface plasmon waves. In inverse conformal map, the black circle in Figure 7b shows the image of the branch point, while the dashed line indicates where v_r goes to infinity.

As field focusing at small cone angles can increase both the field intensity and also the conductive loss, an optimal angle is expected. Conversely, the ratio $-\epsilon_i/\epsilon_r$ of the material determines the energy loss-storage ratio of the system,⁴⁹ and, hence, should determine the global resonant frequency. Contour lines of constant EM field intensification exponent $1 - v_r$ computed from the dispersion relationship for a gold cone with the permittivity model⁵⁰ are shown in Figure 8 for different angles and wavelengths λ of incident light. A global maximum in the intensification exponent exists at $\lambda = 892$ nm, and $\alpha = 11^\circ$. As expected, this global resonant frequency resides at the minimum energy loss-storage ratio of gold, as shown in Figure 8b. The dashed line connects local resonant frequency for different angles, which ends at the global optimal angle. The resonance spectrum for a gold cone at different cone angles is shown in Figure 8a, which shows that broader bandwidth is expected for smaller cone angles.

Asymptotic behavior of $g(\alpha, v)$ in the limit of low conduction loss ($\epsilon_i/\epsilon_r \rightarrow 0$) is most relevant for metals at the visible frequency range. Taylor expansion was carried out about a critical point ($v_o = -1/2 + v_{io}$), which is perturbed in the imaginary eigenvalue near the branch point. Taylor expansion yields $v_r + 1/2 = -i\epsilon_i g_v(v_o, \alpha_o)$. This simplified equation can give a first-order estimate of the dominant exponent v_r , given the permittivity of the metal. Furthermore, it is found at the limit of $\epsilon_r/\epsilon_o \rightarrow -\infty$, that $i\epsilon_r/g(v_o, \alpha_o)$ approaches a constant, and, hence, $v_r + 1/2 \sim -0.693(\epsilon_i/\epsilon_r)$. This estimate reveals that the global resonant frequency occurs at the minimum of ϵ_i/ϵ_r , which is the energy loss-storage ratio of the material.

Intensification exponent calculated from the dispersion relationship can be compared to simulation data published in the literature.⁵¹ Knowing $|E_r| \sim r^{v_r - 1}$, we obtain the dependence of the ratio of the electric field intensity on the exponents and the geometry $E_{\text{tip}}/E_o = (r1/r2)^{v_r - 1}$, where $r1$ is the radial distance from the apex of the cone to the point where E_{tip} is measured, and $r2$ is the radial distance from the apex

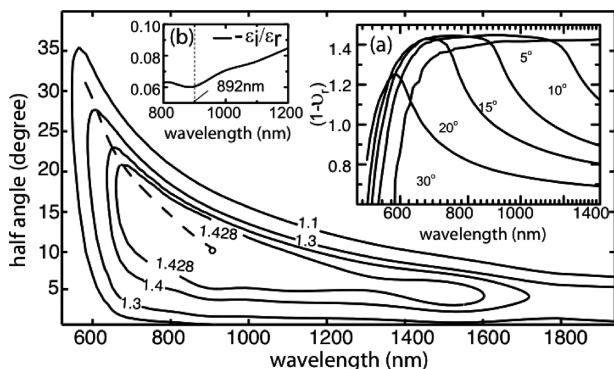


Figure 8. Constant intensification exponent contours lines ($1 - \nu_r = 1.428, 1.4, 1.3, 1.1$) for a gold cone for empirical permittivities,⁵⁰ with different angles and incident light wavelengths, where the dashed curve connects the local resonant conditions from large angles until the global optimal angle (circle).

The inset (a) plots the intensification exponent for a gold cone with different cone angles ($\alpha = 5, 10, 15, 20,$ and 30°) and shows the CPR spectrum broadens and exhibits a redshift away from the planar plasmon resonant wavelength $\lambda_s = c/\omega_s$. The inset (b) plots the ratio of the imaginary to real permittivity for gold,⁵⁰ where maximum intensification occurs at $\lambda = 892$ nm.

to the point where laser with electric field E_0 impinges on the cone. From simple geometry, $r1 = R1 \sin \alpha$ and $r2 = R2 \sin \alpha$ where $R1 = 5$ nm is the radius of curvature of the apex, and $R2 = 300$ nm is the radius of the cylindrical wire at the far end. Figure 9 favorably compares the literature data $\log_{10}(E_{\text{tip}}/E_0)$ to our analytical estimate $(\nu_r - 1) \log_{10}(R1/R2)$, where the exponents are evaluated from the dispersion relationship.

Designing Better Surface Force Instrumentation

Stress singularity is known to occur near moving contact lines⁵² and at contact points of sliding solids. These are non-integrable singularities that must be cutoff by new physics at the contact point, like how microjet removes the singularity of a rounded Taylor cone. Several new physical phenomena can be responsible for such cutoff but one common feature is that the dynamics often exhibit a common stick-slip feature. During evaporation of drops and for force driven wetting, for example, the authors' group has observed molecule and nanocolloid packing at the meniscus to produce stick-slip receding dynamics at the contact line.^{53,54} The singular force field can often induce particle or molecular aggregation or melting and such assembly/disassembly processes are typically hysteretic with a solution manifold like that in Figure 1a.

A common tool for characterizing the roughness of a surface, and to study the "nanorheology" of an assembled molecular layer is surface force apparatus (SFA) spectroscopy.⁵⁵⁻⁵⁹ One classical SFA design (see Figure 10a) is the top cylinder attaching to a stationary spring with the lower cylinder, separated from the upper one with a thin (\sim nm) lubricating film of surfactant molecules below the CMC (critical micelle concentration) pulling laterally at a constant speed or cyclically with a constant speed in each direction.⁵⁵ A curious stick-slip dynamics have been observed recently in a regime bounded by two smooth sliding regimes without

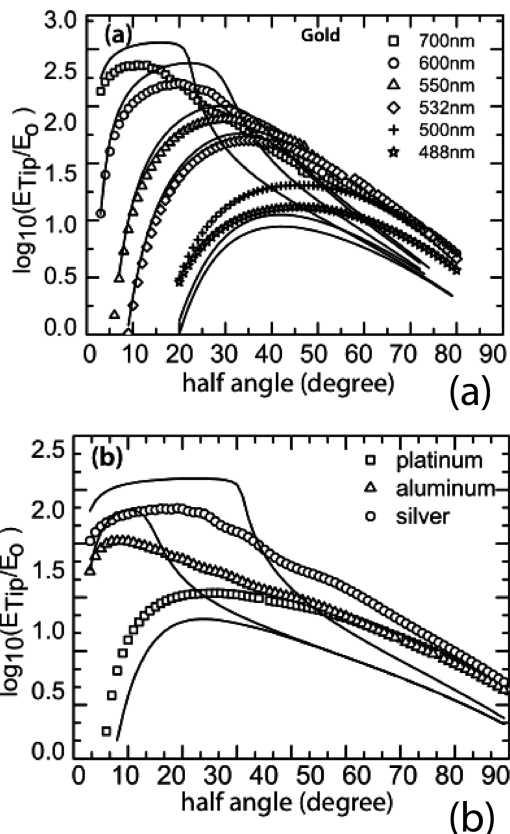


Figure 9. (a) Comparison of theoretical intensification factor $(\nu_r - 1) \log_{10}(R1/R2)$ against the literature values⁵¹ for gold cones of different angles ($R1 = 5$ nm, $R2 = 300$ nm), and (b) Comparison against literature data⁵¹ for three different materials at excitation wavelength 488 nm with the same $R1$ and $R2$.

a static yield stress.^{58,59} The force oscillates between two kinetic states with high- and low-friction forces (viscosities) and shows complex periodic patterns with two oscillation frequencies. This two-frequency stick-slip dynamics occur in an intermediate range of driving velocity for the cylinder (Figures 11 and 12).

It was speculated for some time⁵⁹ that such stick-slip dynamics occur when both a condensed state and a melted state exist for the surfactant monolayer. The cylinder oscillates at its natural spring frequency at low-driving velocities in Figure 12, as the cylinder simply slides over the condensed surfactant monolayer. It also oscillates at the same frequency at high driving speed, when all the surfactant molecules have melted and the film viscosity approaches the low value for a bulk surfactant solution. The interesting hysteresis region exists in the middle, when both melted and condensed states exist.

Like all phase transitions, such phase transitions of surface assemble monolayers are hysteretic with respect to the applied force, describable by the cusp singularity of Figure 1a. In collaboration with Yingxi Zhu, the group has demonstrated with confocal microscopy hysteresis of molecules with respect to a net AC electric force (Figure 10c), which is varied by ramping the AC frequency so that the intensity of dipole due to Debye layer ion conduction changes.⁶⁰ Melting/freezing of the surfactant monolayer in SFA due to the

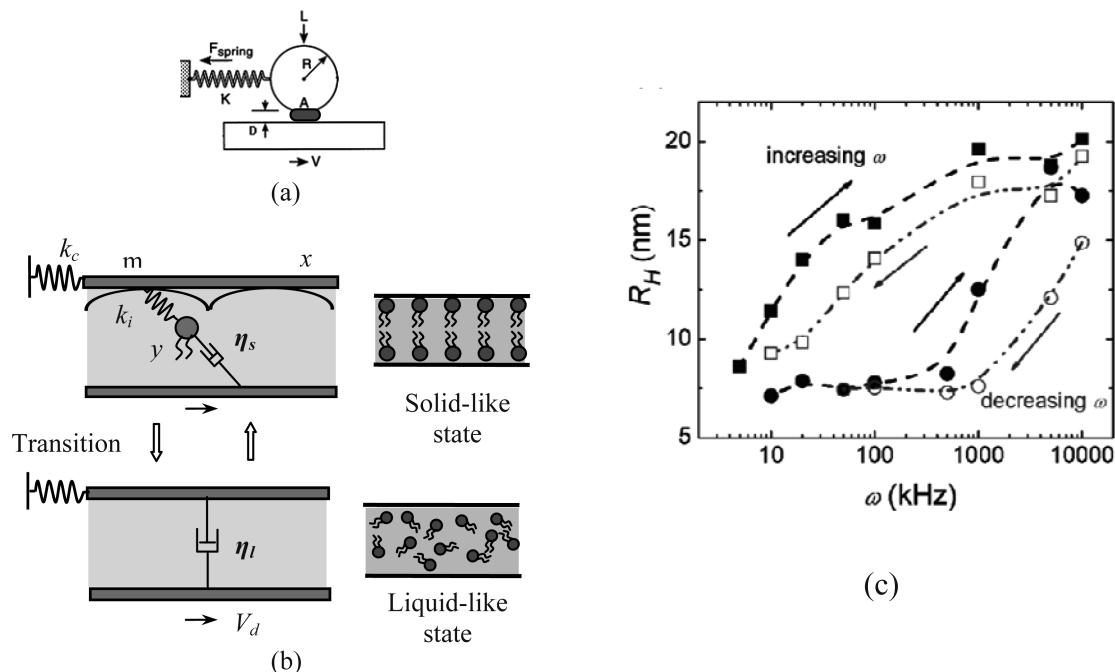


Figure 10. (a) A schematic of the surface force apparatus with a nm-sized lubricated gap between the two cylinders, (b) the single-molecule reduced model for the surfactant molecules within the film.

At low shear rate, it absorbs onto the active site on the mica cylinder. The ensemble of such absorbed molecules forms a solid-like assembled layer of molecules with high viscosity. At high-shear rates, the absorbed molecule is sheared off the surface and its ensemble form a melted state with low viscosity modeled by the usual damper for purely viscous fluids. The transitions from condensed state to/from the melted state is hysteretic, which can be captured by the cusp singularity of Figure 1a, and (c) that force field can change the conformation and phase of molecules was recently verified by varying the field-induced molecular dipole through frequency ramping of the AC field to change the molecular stretching force. Hysteresis in the molecular hydrodynamic radius with respect to the frequency was observed with confocal microscope.⁶⁰

nearly singular hydrodynamic shear is also expected to be hysteretic and its solution manifold resembles the cusp singularity. The different viscosity of each phase is expected to produce a positive feedback mechanism to sustain the jump from one surface to another of the solution manifold in Figure 1a. The limit-cycle and quasi-periodic chaos dynamics suggest that low-dimensional dynamics are at play and singularity theory can be fruitfully applied to reduce the model dimension of the molecular dynamics at the contact point that removes the stress singularity.

With surfactants in the liquid, the assembly surfactant monolayers is precipitated by absorption (trapping) of individual molecules in the potential minima, due to the templating provided by the trapped molecules. The potential minima are due to charged sites on the (mica) cylinder and its maximum electrostatic attraction with the charged surfactants. However, the captured molecules can be sheared off the surface, thus, destroying the monolayer assembly. With a discontinuous jump in the viscosity at the transition between the condensed and melted phase, one then expects that for the intermediate regime of V_d , where both phases exist, a hysteresis exists in the force with respect to V_d , as seen in Figure 12, that is related to the capture and release of a single molecule from the potential minimum by shear. Hence, the condensation and melting of the monolayer assembly can be described by a single molecule in the potential landscape and a convenient way of injecting singularity theory is through a set of coupled equations of motion for a representative master surfactant molecule and the top cylinder

$$M\ddot{x} + k_c x + \frac{\partial U(y-x)}{\partial x} = 0 \quad (3a)$$

$$\eta_s(\dot{y} - V_d) + \frac{\partial U(y-x)}{\partial y} = 0 \quad (3b)$$

where x and y are the lateral position of top cylinder and a surfactant molecule on its surface, M is the mass of top cylinder, k_c is the spring constant. The unknown potential U , with a barrier of U_0 , arises due to the attractive interaction between the periodic lattices of surface charges (spacing a) with the surfactant molecule. It is expected to have sharp minima because of the nature of the (screened) coulombic interaction. V_d is the driving velocity of the bottom cylinder (substrate).

Viscosity of gas and liquid in a nanoslot is a complex phenomenon. For high-Knudsen gas transport in gaps whose height is smaller than the mean free path, the viscosity is dominated by wall collision, particularly low-angle collisions with molecular trajectories almost tangent to the wall.⁶¹ For liquid filled nanoslots, the viscosity is determined by the structure of the liquid molecules and with surfactants, by the self-assembled monolayer. The condensed and melted phases, hence, produce different damping coefficients. Its value for the condensed phase is related to the condensed-phase viscosity μ_s , contact area and gap width $\eta_s = \mu_s A/d$, and its value can be estimated from the shear stress-speed ($\sigma - V_d$) data (in Figure 11) by $\eta_s = \sigma A/V_d$. This viscosity is found to have a wide range $10^3 \sim 10^5 \text{ Pa} \cdot \text{s}$ with strong dependence on the velocity (or shear stress). This suggests that

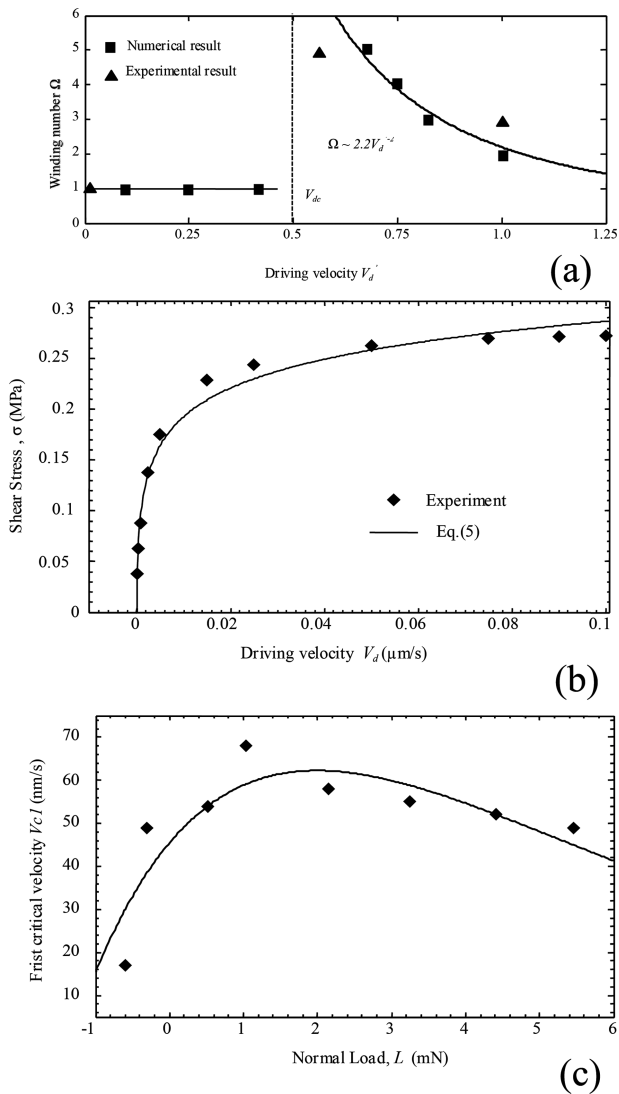


Figure 11. (a) Measured winding number,⁵⁹ the ratio of the two oscillation frequencies, as a function of the velocity of the driving cylinder.

A winding number of one corresponds to a single-frequency limit cycle. Two-frequency oscillations exist beyond a critical driving velocity of about 0.6 ($\mu\text{m/s}$), (b) the stress-velocity curve of (a), and (c) the critical driving velocity as a function of the load-theory (curve) and measured data (points).

there is a shear-thinning effect, as shear from the driving cylinder can move the condensed molecule from the potential minima. We model this shear thinning effect by Kramer's theory for activated transport.⁶² Under an external shear force of $F_e \sim \sigma A/N$, the forward and backward hopping frequencies out of a potential well of a single molecule are given by the rate equation $\omega_{\pm} = \omega_0 e^{\frac{U_0 \pm \sigma A a / 2N}{k_B T}}$. The prefactor ω_0 is the vibration frequency of the water molecule inside the potential well $\omega_0 = U_0 / (a^2 \eta_{ib})$, where $\eta_{ib} \sim 6 \pi \mu_1 D$ is the damping coefficient for a single molecule with size D in a bulk solvent viscosity of μ_1 . With the net forward hopping frequency being $\omega_+ - \omega_-$, the average surfactant drift velocity is $V_m = a(\omega_+ - \omega_-)$. At steady transport, this fluid velocity is expected to be proportional to (but is a small fraction of) the driving velocity and we have

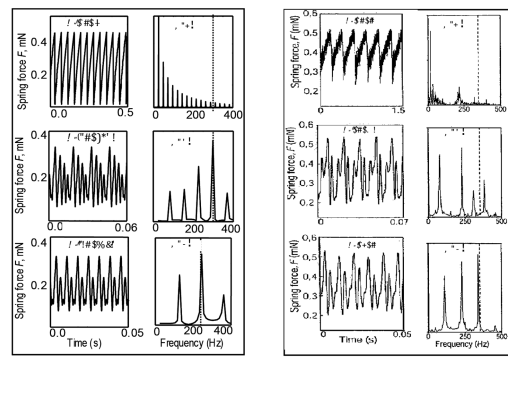
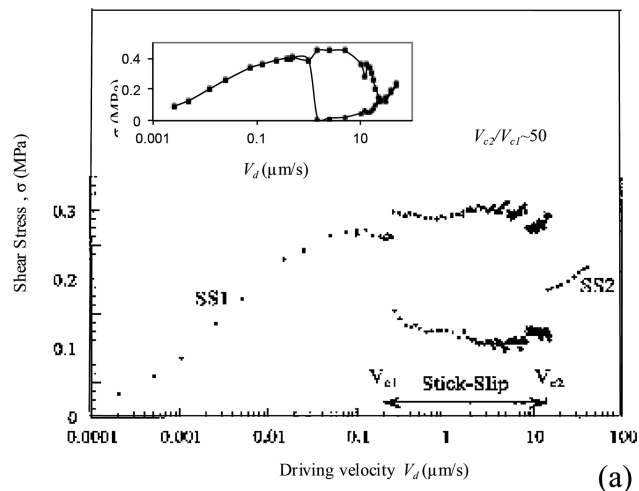


Figure 12. (a) Observed and simulated (inset) solutions, and (b) Measured and simulated force oscillations and power spectra.

$$V_d = c_1 V_m = \frac{2c_1 U_0}{\eta_{ib} a} e^{\frac{U_0}{k_B T}} \sinh\left(\frac{\sigma \tilde{V}}{k_B T}\right) \quad (4)$$

with a proportionality constant $c_1 \gg 1$ and a molecular volume $\tilde{V} = Aa/2N$. The condensed phase viscosity is then estimated as

$$\mu_s = \frac{\sigma}{(V_d - V_m)/d} \approx \frac{\sigma d \eta_{ib} a}{c_1 2U_0} e^{\frac{U_0}{k_B T}} \text{csch}\left(\frac{\sigma \tilde{V}}{k_B T}\right) \quad (5)$$

Equation 4 is in good agreement with the condensed (high-friction) smooth sliding stress-speed ($\sigma - V_d$) data,⁵⁹ as shown in Figure 11b for a normal load of $L = 4.5 \text{ mN}$ between the two mica cylinders with surfactant at a concentration of 0.8 CMC and at a temperature of 20°C. The force increases linearly at low-speed V_d , but logarithmically at high V_d .

The melted film with mobile surfactant molecules is assumed to have the same rheological property as a free bulk surfactant solution that feels no surface force. The dynamics of the molecule in 3b can then be omitted and viscous drag from the sliding cylinder is now transmitted directly to the top cylinder and we modify its equation of motion in 3a to

$$M\ddot{x} + \eta_l(\dot{x} - V_d) + k_c x = 0 \quad (6)$$

Where $\eta_l = \mu_1 A/d \sim 10 \text{ Pa} \cdot \text{m} \cdot \text{s}$ is the damping coefficient and is also estimated by the shear stress-velocity

relation ($\sigma-V_d$) in the melted smooth sliding region in Figures 11b and 12.

The key issue of which phase exists under a specific shear must be addressed by examining how a molecule is captured and released by the sites on the surface. The lattice site in front of the molecule exerts a force in the direction of the viscous drag while the force due to the site behind it opposes viscous drag. However, because the molecule moves slower in front of a site than behind it for the same reason, it favors the former position and the time-averaged net force on the molecule is attractive. Also, as the viscosity for each phase is different, the critical shear (or sliding velocity V_d) for the stick-slip transition, when the molecule is dragged off the lattice site, is lower than the slip-stick transition, when it is recaptured by the lattice site. The actual molecular velocity is a linear combination of its average velocity V_m and a fluctuation due to viscous drag from the periodic lattice $\dot{z}=V_m+\tilde{v}$, where $z=y-x$ is the relative position of the molecule relative to the stationary cylinder and $\tilde{v}=f(z)/\eta_s$ arises from the local surface force. This force $f(z)=-\frac{\partial U(z)}{\partial z}$ has a zero average over one unit cell $\langle f(z) \rangle = -\frac{1}{a} \int_a \frac{\partial U}{\partial z} dz = 0$.

The distribution $p(z)$ of the molecule over a unit cell of length a is then $p(z) \sim \frac{V_m}{a} \frac{dz}{dz} \sim \frac{1}{a} \left(\frac{1}{1+\tilde{v}/V_m} \right) \sim \frac{1}{a} (1-\tilde{v}/V_m)$. Although $\langle \tilde{v} \rangle = \langle f \rangle = 0$, the average force weighted by this drift-induced inhomogeneous distribution is quadratic in f and has a nonzero average. This average force for a drifting velocity is $f_M = \langle p(z)f(z) \rangle \sim -\frac{1}{V_m \eta_s a^2} \langle f^2(z) \rangle \sim \frac{\alpha(L)}{V_d}$. The exact profile of the surface force potential $f(z)$ is difficult to obtain but the fact that f_M scales inversely with respect to V_d is sufficient for the estimate of the critical velocities. The parameter $\alpha(L)$ depends on the exact potential profile and lattice geometry/spacing.

The condensed high-friction smooth sliding mode becomes unstable at $V_d = V_{c1}$ when the viscous drag $\eta_s V_d$ exceeds f_M . This critical force is defined as $f_{slip} = \eta_s V_{c1}$, where $V_{c1} = \sqrt{\alpha/\eta_s}$ (7) by balancing the viscous drag with f_M . For a normal load of $L = 4.5\text{mN}$, and an estimated damping coefficient of $\eta_s \sim 10^3 \text{ Pa}\cdot\text{m}\cdot\text{s}$ at $V_d = V_{c1} = 0.3 \mu\text{m/s}$, we estimate α to be 0.15 nJ . The low-friction smooth sliding mode loses its stability at the second critical velocity $V_d = V_{c2} = 14\text{--}17 \mu\text{m/s}$ when f_M/N becomes smaller than the viscous drag of one bulk molecule at the middle of film, $6\pi\mu_1 DV_{c1}/2$ with a molecule size of $D \sim 1 \text{ nm}$, and the viscosity of $\mu_1 \sim 10 \text{ P}\cdot\text{s}$. This critical force is defined as $f_{stick} = 6\pi\mu_1 DNV_{c1}/2$. Simple proportionality exists for the two critical velocities $(V_{c2}/V_{c1}) \sim (\eta_s/ND\mu_1)^{0.5} \sim 10^2$, which is close to the measured value of 50 in Figure 12.

The dynamics within the stick-slip regime can now be simulated with Eqs. (3) and (6) with the following criteria:

- the governing equation is switched from Eqs. (3) to (6) if $y-x > a$ when the molecule exits one potential minimum; and
- from Eqs. (6) to (3) when $f_{stick} > 6\pi\mu_1 DNV_{c1}/2$, and the molecule is recaptured by a site.

In invoking “sticking” condition (b), the velocity difference between the two cylinders $\Delta V = V_d - \dot{x}$ is monitored during the simulation and must be decreasing. The critical force $f_{stick} = 6\pi\mu_1 DNV_{c1}/2$ is specified by the first critical velocity in (7). It is noted that the “melting” condition (a) differs from that used to determine the stability of the stick phase—this dynamic hysteretic condition allows cylinder inertia to

correct the critical force for “melting”. The simulations produce both the one-frequency and two-frequency stick-slip dynamics, with quantitatively accurate spring force time series and power spectra, at the correct values of the driving velocity); the correct frequency ratio (Figure 11), and the complete force-speed data in both the stable sliding regions and the stick-slip region (Figure 12).

The model offered by Singularity theory has allowed us to capture the stick-slip dynamics that relieve the stress singularities at the contacting solids. It is the shear-induced melting of the surfactant molecules from the potential minima that relieves the stress. However, with lower viscosity, the inertia of the spring-cylinder system produces cylinder oscillations. The velocity of the driving cylinder approaches zero at the extremes of the oscillation and the vanishing shear returns the surfactant molecules to the potential minima—the monolayer recondenses. In addition to the natural frequency of the cylinder at the melted state, this stick-slip dynamics exhibit another frequency corresponding to the escape and capture time of the surfactant molecule at the potential minimum.

Summary

These disparate projects from the authors’ group have all benefited from a common mathematical framework for geometric or parametric singularities. In many cases, such as the nanocolloid mass spectrometry, knowledge of such theory precedes the experimental outcome. In other cases, like stick-slip dynamics at a contact singularity, the theory explains an existing phenomenon. In yet another case, like the fast igniting converters, the theory allows us to design new technologies without experiments or computations. The Taylor cone and cone plasmonic problems are particularly intriguing, as the field focusing effect singular geometry selects dominant modes that are themselves singular and the singularities of the Riemann manifold allow the dominant modes to offer accurate quantitative description of the solution. We had singularities galore!

Acknowledgment

The senior author is grateful to Neal Amundson for imbuing him with the ideal espoused here and to all his students and collaborators who share his excitement about singularities. Part of this work is supported by NSF grants IDBR0852741 and CBET 1065652.

Literature Cited

- Chang HC, Calo JM. Exact criteria for uniqueness and multiplicity of an n th order chemical reaction via a catastrophe theory approach. *Chem Eng Sci.* 1979;34:285–299.
- Ben Y, Demekhin EA, Chang HC. A spectral theory for small-amplitude miscible fingering. *Phys Fluids.* 2002;14:999–1006.
- Chang HC. Evolution of nonlinear waves on vertically falling films—a normal form analysis. *Chem Eng Sci.* 1987;42:515–533.
- Chen LH, Chang HC. Nonlinear waves on liquid film surfaces—II. Bifurcation analyses of the long-wave equation. *Chem Eng Sci.* 1986;41:2477–2486.
- Lahbabi A, Chang HC. Flow in periodically constricted tubes: transition to inertial and nonsteady flows. *Chem Eng Sci.* 1986;41:2487–2505.
- Chang HC, Demekhin EA. *Complex Wave Dynamics on Thin Film.* Elsevier Science; 2002.
- Chang HC, Demekhin EA, Kalaidin E. Interaction dynamics of solitary waves on a falling film. *J Fluid Mech.* 1995;294:123–154.

8. Chang HC, Demekhin EA, Kopelevich DI. Stability of a solitary pulse against wave packet disturbances in an active medium. *Phys Rev Lett*. 1995;75:1747–1750.
9. Ye Y, Chang HC. A spectral theory for fingering on a prewetted plane. *Phys Fluid*. 1999;11:2494–2515.
10. Yuzhakov VV, Miller AE, Chang HC. Pattern formation during electropolishing. *Phys Rev B*. 1997; 56:12608–12624.
11. Thamida SK, Chang HC. Nanoscale pore formation dynamics during aluminum anodization. *Chaos*. 2002;12:240–251.
12. Boe E, Chang HC. Dynamics of delayed systems under feedback control. *Chem Eng Sci*. 44, 1281 (1989).
13. Chen CC, Chang HC. Accelerated disturbance damping of an unknown distributed system by nonlinear feedback. *AIChE J*. 1992;38:1461–1476.
14. Sen M, Chang HC. Gas Research Institute. Process and apparatus for enhancing in-tube heat transfer by chaotic mixing. U.S. Patent 5,311,932. May 17, 1994.
15. Archaya N, Sen M, Chang HC. Analysis of heat transfer enhancement in coiled-tube heat exchangers. *Int J Heat Mass Tran*. 2001;44:3189–3199.
16. Keith JM, Chang HC, Leighton DT. Designing a fast-igniting catalytic converter system. *AIChE J*. 2001;47:650–663.
17. Leighton DT, Chang HC. A theory for fast-igniting catalytic converters. *AIChE J*. 1995;41:1898–1914.
18. Chang HC, Yeo LY. *Electrokinetically Driven Microfluidics and Nanofluidics*. New York, NY: Cambridge University Press; 2010.
19. Balakotaiah V, Chang HC. Dispersion of chemical solutes in chromatographs and reactors. *Phil Trans R. Soc Lond A*. 1995;351:1695–39–75.
20. Leighton DT, Chang HC. Fast-igniting catalytic converters with bypass. U.S. Patent No. 6,428,754. August 6, 2002.
21. Zheng H, Keith JM. Averaging theory for diesel particulate filter regeneration. *AIChE J*. 2007;53:1316–1324.
22. Taylor GI. Disintegration of water drops in an electric field. *Proc R Soc A*. 1964;280:383–397.
23. Marginean I, Nemes P, Vertes A. A stable regime in electrosprays. *Phys Rev E*. 2007;76:026320–026325.
24. Fenn JB, Mann M, Meng CK, Wong SF, Whitehouse CM. Electrospray ionization for mass spectrometry of large biomolecules. *Science*. 1989;246:64–71.
25. Page JS, Kelly RT, Tang K, Smith RD. Ionization and transmission efficiency in an electrospray ionization-mass spectrometry interface. *J Amer Soc Mass Spectrom*. 2007;18:1582–1590.
26. Zeleny J. Instability of electrified liquid surface. *Phys Rev*. 1917;10:1–6.
27. Wang Y, Tan MK, Go DB, Chang HC. Electrospray cone-jet breakup and droplet production for electrolyte solutions. *Europhys Lett*. 2012;99:64003. (Editor's highlight).
28. Cheng X, Chang HC. Universal nanocolloid deposition patterns: can you see the harmonics of a Taylor cone? *J New Phys*. 2009;11:75023–75031.
29. Cheng X, Chang HC. Identification and separation of DNA-hybridized nanocolloids by Taylor cone harmonics. *Electrophoresis*. 2009;30: 3236–3241.
30. Chetwani N, Maheshwari S, Chang HC. Universal cone angle of ac electrosprays due to net charge entrainment. *Phys Rev Lett*. 2008;101:204501.
31. Chetwani N, Cassou CA, Go DB, Chang HC. Frequency dependence of alternating current electrospray ionization mass spectrometry. *Anal Chem*. 2011;83:3017–3023.
32. Yeo L, Gagnon Z, Chang HC. AC Electrospray biomaterial synthesis. *Biomaterials*. 2005;26:6122.
33. Maheshwari S, Chang HC. Assembly of multi-stranded nanofiber threads through ac electrospinning. *Adv Mater*. 2009;21:349–354.
34. Gagnon Z, Chang HC. Dielectrophoresis of ionized gas microbubbles: dipole reversal due to diffusive double layer polarization. *Appl Phys Lett*. 2008;93:224101.
35. Ho J, Tan MK, Go DB, Friend JR, Chang, HC. A paper-based microfluidic surface acoustic wave sample delivery and ionization source for rapid and sensitive ambient mass spectrometry. *Anal Chem*. 2001;83: 3260–3266.
36. Basuray S, Chang HC. Induced dipoles and dielectrophoresis of nano-colloids in electrolytes. *Phys Rev E*. 2007;75:060501–060504.
37. Yossifon G, Chang HC. Selection of nonequilibrium overlimiting currents: universal depletion layer formation dynamics and vortex instability. *Phys Rev Lett*. 2008;101:254501.
38. Chang HC, Yossifon G. Understanding electrokinetics at the nanoscale—a perspective. *Biomeicrofluidics*. 2009;3:012001.
39. Cheng IF, Senapati S, Cheng X, Basuray S, Chang HC, Chang HC. A rapid field-use assay for mismatch number and location of hybridized DNAs. *Lab Chip*. 2010;10:828–831.
40. Zhou R, Chang HC, Protasenko V, Kuno M, Singh AK, Jena D. CdSe nanowires with illumination enhanced conductivity: induced dipoles, dielectrophoretic assembly and field-sensitive assembly. *J App Phys*. 2007;101:073704.
41. Zhou R, Wang P, Chang HC. Bacteria capture, concentration and detection by AC dielectrophoresis and self-assembly of dispersed single-wall carbon nanotubes. *Electrophoresis*. 2006;27:1375.
42. Basuray S, Senapati S, Aijian A, Mahon AR, Chang HC, Shear, AC Field. Enhanced carbon nanotube impedance assay for rapid, sensitive and mismatch-discriminating DNA hybridization. *ACS Nano*. 2009;3: 1823.
43. Gagnon Z, Senapati S, Gordon J, Chang HC. Dielectrophoretic detection and quantification of hybridized dna molecules on nanogenetic beads. *Electrophoresis*. 2008;29:4808.
44. Chang HC, Nanobead electrokinetics: the enabling microfluidic platform for rapid multi-target detection. *AIChE J*. 2007;53:2486–2492.
45. Basuray S, Wei HH, Chang HC. Dynamic double-layer effects on ac-induced dipoles of dielectric nanocolloids. *Biomeicrofluidics*. 2010;4:022801.
46. Basuray S, Chang HC. Designing a sensitive and quantifiable nanocolloid assay with dielectrophoretic cross-over frequency. *Biomeicrofluidics*. 2010;4:013205.
47. Wang Y, Plouraboue F, Chang HC. Broadband converging plasmon resonance at a conical nanotip. *Opt Express*. 2013;21:6609–6617.
48. Kawata Y, Xu C, Denk W. Feasibility of molecular-resolution fluorescence near-field microscopy using multi-photon absorption and field enhancement near a sharp tip. *J Appl Phys*. 1999;85:1294–1301.
49. Wang F, Shen Y. General properties of local plasmons in metal nanostructures. *Phys Rev Lett*. 2006;97:206806.
50. Johnson PB, Christy RW. Optical constants of the noble metals. *Phys Rev B*. 1972;6:4370.
51. Issa NA, Guckenberger R. Optical nanofocusing on tapered metallic waveguides. *Plasmonics*. 2007;2:31.
52. Huh C, Scriven LE. Hydrodynamic model of steady movement of a solid/liquid/fluid contact line. *J Colloid Interf Sci*. 1971;35:85–101.
53. Maheshwari S, Zhang L, Zhu Y, Chang HC. Coupling between precipitation and contact-line dynamics: multiring stains and stick-slip motion. *Phys Rev Lett*. 2008;100:044503.
54. Veretennikov I, Agarwal A, Indeikina A, Chang HC. Unusual contact-line dynamics of thick films and drop. *J Colloid Interf Sci*. 1999;215:425.
55. Yoshizawa H, Chen YL, Israelachvili J. Fundamental mechanisms of interfacial friction. 1. Relation between adhesion and friction. *J Phys Chem*. 1993;97:4128.
56. Klein J, Kumacheva E. Simple liquids confined to molecularly thin layers. I. Confinement-induced liquid-to-solid phase transitions. *J Chem Phys*. 1998;108:6996.
57. Demirel AL, Granick S. Friction fluctuations and friction memory in stick-slip motion. *Phys Rev Lett*. 1996;77: 4330.
58. Richetti P, Drummond C, Israelachvili J, In M, Zana R. Inverted stick-slip friction. *Europhys Lett*. 2001;55:653.
59. Drummond C, Israelachvili J, Richetti P. Friction between two weakly adhering boundary lubricated surfaces in water. *Phys Rev E*. 2003;67:066110.
60. Wang S, Chang HC, Zhu Y. Hysteretic conformational transition of single flexible polyelectrolyte under resonant ac electric polarization. *Macromol*. 2010;43:7402–7405.
61. Arya G, Chang HC, Maginn EJ, Knudsen diffusivity of a hard sphere in a rough slit pore. *Phys Rev Lett*. 2003;91:26102.
62. Kramer HA. Brownian motion in a field of force and the diffusion model of chemical reactions. *Physica*. 1940;7:284.

Manuscript received Sept. 13, 2012, and revision received Mar. 3, 2013.